Nitric Oxide Chemistry Effects in Hypersonic Boundary Layers

C. J. Arisman[1], C.T. Johansen[2], W.C. Galuppo[3], A. McPhail[3]
University of Calgary, Calgary, AB, T2N 1N4

Simulations of gas seeding into a hypersonic boundary layer flow were performed using OpenFOAM to investigate and quantify errors associated with quantitative planar laser induced fluorescence thermometry and velocimetry techniques. The compressible rhoCentralFoam solver was modified to include multiple species transport and chemical reactions. Simulations replicated conditions used in NASA Langley's 31" Mach 10 facility with a wedge model oriented at various angles of attack with respect to the freestream flow in the test section. OpenFOAM predictions were compared to ANSYS Fluent v6.3 simulation results. The seeded gas, seeding flow rate and the wedge angle of attack were varied in the simulations. Adverse chemistry effects from the reaction of nitric oxide with molecular oxygen were investigated at various facility running conditions. Specifically, the effect of heat release on velocity and temperature profiles that would be obtained using the non-intrusive laser measurement techniques was assessed.

Nomenclature

ρ	=	density
u	=	velocity
P	=	pressure
μ	=	viscosity
h_s	=	sensible enthalpy
I	=	unit tensor
α	=	thermal diffusivity
k	=	thermal conductivity
c_p	=	specific heat at constant pressure
S_h	=	enthalpy source term
Y_i	=	mass fraction of species i
R_i	=	generation of species i due to chemical reaction
T	=	temperature
NO	=	nitric oxide
I_2	=	iodine
Kr	=	krypton
NO_2	=	nitrogen dioxide
O_2	=	oxygen
R	=	universal gas constant
$[NO]$	=	concentration of nitric oxide
$[NO_2]$	=	concentration of nitrogen dioxide
$[O_2]$	=	concentration of oxygen
$t_{1/2}$	=	half-life
k_{NO}	=	reaction rate of nitric oxide
X_{NO}	=	mol fraction of nitric oxide
X_{O2}	=	mol fraction of oxygen
M	=	Mach number
γ	=	ratio of specific heats

[1] Graduate Student, Department of Mechanical and Manufacturing Engineering.
[2] Assistant Professor, Department of Mechanical and Manufacturing Engineering, Member AIAA.
[3] Undergraduate Student, Department of Mechanical and Manufacturing Engineering.

θ = angle of plate with respect to free stream
β = oblique shock angle with respect to free stream

I. Introduction

THE transition to turbulence in hypersonic flows can significantly increase the heat transfer rate to the surface of flight vehicles and poses a serious risk to thermal protection systems.[1] In a 2008 review of transition to turbulence in hypersonic flows, Schneider states that the instability mechanisms that lead to transition, which differ from the mechanisms at subsonic speeds, are still poorly understood.[2] These mechanisms include the concave-wall Görtler instability,[3] the first and second mode Mack instabilities,[4] and the three-dimensional crossflow instability.[5,6] Moreover, it has been shown experimentally that the presence of surface roughness or discrete protuberances on the surface shortens the transition length. Unfortunately, there is no general mechanism-based theory to determine the conditions under which roughness can cause transition.[3] Since vehicle design tools rely on computational fluid dynamics (CFD), relevant experimental data is critical for numerical model validation.

These concerns motivated a series of hypersonic wind tunnel experiments in NASA Langley Research Center's 31-inch Mach 10 Air Tunnel facility to study this problem.[7-10] Figure 1 shows a schematic of the wind tunnel facility, the test section, and the planar laser-induced fluorescence (PLIF) systems.

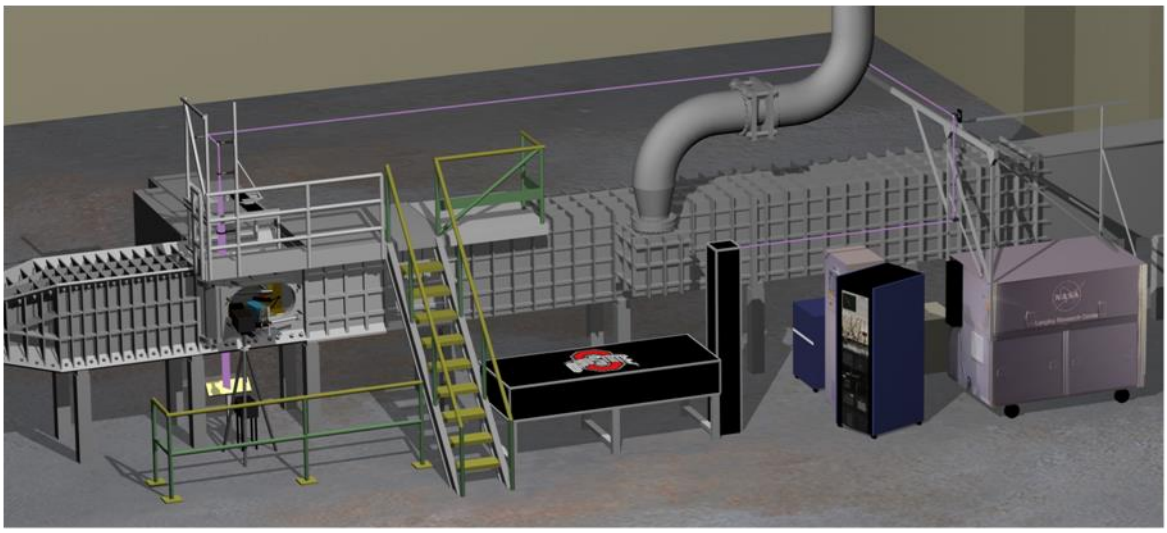

Figure 1. NASA Langley 31" Mach 10 Air Tunnel Facility with PLIF systems. Reproduced from Ref [7]

In these experiments, a planar, 20 degree wedge was placed into the test section and nitric oxide (NO) gas was seeded through a slot on the model to allow for PLIF images to be obtained downstream. A series of protuberance shapes with various heights were placed on the wedge surface and PLIF flow visualization and quantitative molecular tagging velocimetry (MTV) measurements were obtained. Figue 2 shows the wedge model, gas seeding slot, and a cylindrical trip that was used during several of the experiments.[7] In this facility, the wind tunnel stagnation pressure and model angle of attack (AoA) can be varied to replicate different edge conditions, including Reynolds number, on the wedge surface.

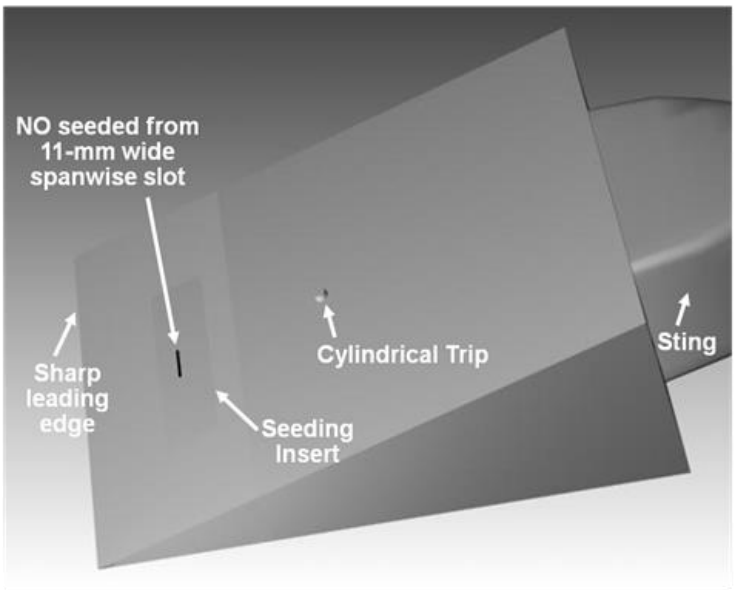

Figure 2. Schematic of wedge model, indicating the gas seeding slot and a cylindrical-shaped trip. Reproduced from Ref [7]

With any experimental measurement technique there are concerns with flow contamination caused by diagnostics. In high-speed flows, physical probes can cause large aerodynamic disturbances. Moreover, they typically only collect data at a limited number of discrete spatial points in the flow. Laser-based techniques combined with high-speed video cameras are both non-intrusive and can collect large amounts of data at many positions. The gas seeding process required for NO PLIF, however, does introduce artificial aerodynamic perturbations, alters the flow properties, and may react chemically with the surrounding oxygen. However, these artificial effects can be reduced and nearly eliminated by decreasing the seeding flow rate. Since a reduction in seeding flow rate results in a decreased signal-to-noise ratio in the PLIF images and results in a smaller penetration distance of the seed gas into the boundary layer, an optimum flow rate needs to be determined.

The need to quantify negative effects associated with the gas seeding process motivated a numerical study comparing several typical PLIF seed gases injected from the wedge model.[11] The gases simulated included NO, Krypton (Kr), and Iodine (I_2). Although Kr and I_2 are non-reactive with oxygen, they have a much higher molecular weight (MW) than NO and air, resulting in large differences in their respective thermo-physical properties. For a given mass flow rate of seeded gas, it was found that NO had the largest dispersion rate and penetrated the furthest into the boundary layer. In addition, NO had the smallest adverse effect on velocity and temperature profiles downstream. The study, however, did not investigate the effects of model AoA, facility stagnation pressure, or chemistry effects of NO on the boundary layer profiles. Therefore, the focus of the current study is to investigate these effects and to also compare results between two CFD codes. A methodology of assessing these effects analytically is also presented.

II. CFD Solver

The open source CFD software, OpenFOAM v2.1, was used with a modified version of the rhoCentralFoam solver for the simulations. Direct Simulation Monte Carlo (DSMC) FOAM and rhoCentralFoam are the only solvers distributed with OpenFOAM v2.1 that are capable of accurately simulating hypersonic flows. DSMC simulations calculate the collisions between particles in a probabilistic manner and are typically very computationally expensive. In contrast, rhoCentralFoam solves the Navier Stokes (continuum) governing equations, which reduces the computational load but is inaccurate in predicting rarefied flows. The freestream Knudsen number, which is the ratio of the mean free path to a characteristic length scale, is estimated to be approximately Kn = 0.003 in NASA's 31-inch Mach 10 facility (P_{stag} = 350 psi). Therefore, the flow is not considered to be rarefied (Kn < 0.01) and the DSMC solver is not required.

Compared to the other Navier Stokes solvers available in OpenFOAM, rhoCentralFoam includes the dissipation function in the energy equation, which is required to predict viscous heating near wall boundaries. The solver also accurately simulates flow discontinuities (e.g. shock waves) through the use of a custom central finite volume

discretization scheme.[12] The central scheme is based on the work by Nessyahu and Tadmor[13] but is semi-discrete and non-staggered, such that it can operate with collocated meshes as developed by Kurganov and Tadmor (KT).[14] This type of scheme was developed since solution variables, such as velocity and pressure, are often collocated in popular CFD software packages, including ANSYS Fluent and OpenFOAM. The advantage of the central scheme over OpenFOAM's other schemes is that it can produce non-oscillatory solutions near flow discontinuities. Examples of other numerical schemes that can accurately treat flow discontinuities include the monotone upstream-centered schemes for conservation laws,[15] piecewise parabolic method (PPM),[16] essentially non-oscillatory (ENO) schemes,[17] weighted ENO (WENO) schemes,[18] and the Runge-Kutta discontinuous Galerkin (RKDG) method.[19] None of these are available in any of the OpenFOAM v2.1 solvers. A detailed description of rhoCentralFoam can be found in Ref. [12] where rhoCentralFoam has been used to solve supersonic flow over a forward facing step, supersonic jet, and shock tube.[12]

The solver in its standard form does not include the capability to simulate species transport or include chemical reactions. A modified version has been used to solve radiation associated with hypersonic flows around re-entry vehicles.[20] A similar compressible OpenFOAM solver developed by Fureby *et al*. has been used to simulate supersonic combustion and gaseous explosions.[21]

A. Governing Equations

In its standard form, rhoCentralFoam solves the unsteady, compressible Navier-Stokes equations for both laminar and turbulent flows. The standard rhoCentralFoam solver has been modified to create the rhoCentralReactingFoam solver. The conservation of mass, momentum (neglecting body forces), and energy used by the rhoCentralReactingFoam solver are defined as:

$$\frac{\partial \rho}{\partial t} + \nabla \cdot (\rho u) = 0 \tag{1}$$

$$\frac{\partial (\rho u)}{\partial t} + \nabla \cdot (\rho u^2) = -\nabla P + \nabla \cdot \tau \tag{2}$$

$$\frac{\partial (\rho h_s)}{\partial t} + \nabla \cdot (\rho u h_s) = \nabla \cdot [\alpha \nabla h_s + \sum_{i=1}^{n} h_i J_i] + \frac{DP}{Dt} + \nabla \cdot (\tau \cdot u) + S_h \tag{3}$$

where ρ, u, P, h_s, T, S_h are the gas density, velocity, pressure, sensible enthalpy, temperature and enthalpy source respectively. α is the thermal diffusivity and is defined as $\frac{k}{c_p}$ where k is the thermal conductivity and c_p is the specific heat at constant pressure. The viscous stress tensor, τ, in vector form is defined as:

$$\tau = \mu(\nabla u + (\nabla u)^T - \frac{2}{3}\nabla \cdot uI) \tag{4}$$

where μ is the viscosity and I is the unit tensor. The viscous stress tensor is 2μ multiplied by the deviatoric component of the deformation gradient tensor.

The solver handles viscous effects by first solving the inviscid equation and using the inviscid solution as a predictor for the viscous solution, correcting for the diffusive terms.[12] The solver is unsteady and steady state solutions are obtained by marching forward in time until fluctuations in flow variables no longer subsist.[12] Since the Reynolds number of the flow, based on the freestream velocity and plate length, is small (Re = 3.4e5), turbulence modeling is not required in the simulations. However, rhoCentralFoam does have the ability to use built-in Reynolds Averaged Navier Stokes (RANS) and Large Eddy Simulation (LES) turbulence models for higher Reynolds number flows.

Because the rhoCentralFoam solver is limited to single species non-reacting flows in its standard form, modifications were implemented to expand its capability and solve this hypersonic, reacting flow. In order to use it to investigate gas seeding, multiple species transport and multi-component diffusion were added. A chemical reaction source term in the energy equation along with Arrhenius rate chemistry has been implemented to investigate the effects of NO reacting with O_2 in the flow. Implementation of these features is based on the structure of the available solver, reactingFoam.[22] The transport of multiple species mass fraction (Y_i) is given by the following conservation equation:

$$\frac{\partial(\rho Y_i)}{\partial t} + \nabla \cdot (\rho u Y_i) = -\nabla \cdot J_i + R_i \tag{5}$$

where J_i is the diffusion flux of species *i* and is defined as:

$$J_i = -\rho D_{i,m} \nabla Y_i \tag{6}$$

The diffusion coefficient, $D_{i,m}$, for species *i* in the mixture is determined from the Chapman-Enskogg equation.[23, 24] In simulations where only two species were simulated, a binary diffusion coefficient was calculated:

$$D_{i,m} = 0.00188 \frac{\left[T^3 \left(\frac{1}{M_a} + \frac{1}{M_b}\right)\right]^{\frac{1}{2}}}{P \sigma_{ab}^2 \Omega_d} \tag{7}$$

where σ_{ab} is the average species collision cross section based on tabulated values published by Svehla[25] and Ω_d is the diffusion collision integral. For the diffusion coefficient calculation *P* is in bar. M_a and M_b are the molecular weights of species a and b respectively.

Other modifications were made to the energy equation. While the standard rhoCentralFoam solver computes the transport of total energy, the modified version solves the sensible enthalpy equation (Eq. (3)) in order to easily include the chemical reaction and species transport terms from the reactingFoam solver. In addition, the standard rhoCentralFoam solver uses a unity Prandlt number assumption in the energy equation, whereas the modified solver allows for a variable Prandtl number. This was implemented by including a variable thermal conductivity term directly into the energy equation. The thermal conductivity is calculated from a temperature dependent polynomial curve fit to a modified Euken correction equation taken from the work of Hollis:[26]

$$k = \mu \left(\frac{15}{4} - 1.32 \left(\frac{c_p}{R} - \frac{5}{2} \right) \right) R \tag{8}$$

Specific heat values for NO were taken from the NIST-NAJAF tables.[27] The enthalpy transport term has also been included in the energy equation as the Lewis number is no longer unity due to the Prandlt and Schmidt numbers being allowed to vary for the flow. The viscosity is calculated based on kinetic theory from the Chapman-Cowling relationship also found in the work by Hollis:[26]

$$\mu = 2.6693 * 10^6 \frac{\sqrt{MT}}{\sigma \Omega_d} \tag{9}$$

Mixture properties are calculated based on a mass weighted average of the individual species properties.

The standard reactingFOAM solver assumes a unity Schmidt number in the species conservation equation. Since a variable Schmidt number is required for the current simulation, individual species diffusion coefficients have been included in the species conservation equation. The rhoCentralReactingFoam solver uses the Maxwell-Steffan equations for the calculation of diffusion coefficients for multi-species mixtures and the Chapman-Enskogg equation (Eq. (7)) for the binary diffusion coefficient.

B. Simulation Setup

The computational domain is based on the wedge model (Fig. 2) used in the experiments performed in NASA Langley's 31-inch Mach 10 facility (Fig. 1). A schematic of the computational domain relative to the wedge model and sting is shown in Fig. 3. The domain is two dimensional, 200 mm in length (*x* direction) and 30 mm in height (*y* direction). The origin of the coordinate system is at the leading edge of the wedge. The gas is seeded from a slot that is 0.81 mm thick and 11 mm wide located 29.4 mm downstream of the leading edge.

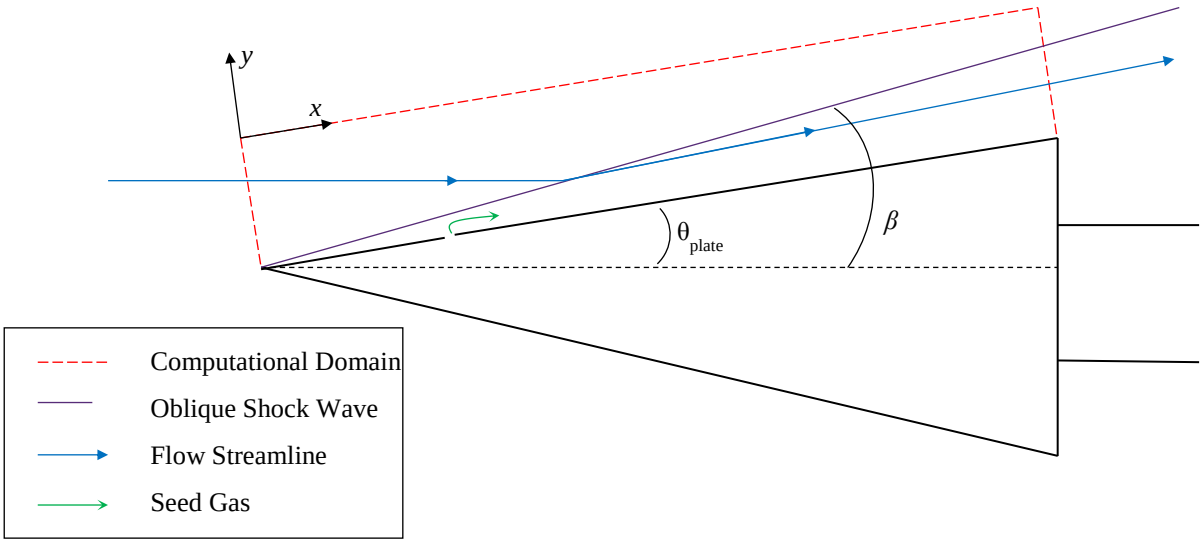

Figure 3. Computational domain

The bottom of the domain is aligned with the top surface of the wedge. Changes in plate angle (θ_{plate}) are controlled by specifying the inlet velocity (direction) on the top and left boundaries. Constant pressure, temperature, and velocity values of P = 68.4 Pa, T = 52.3 K, and U = 1407.3 m/s (Ma = 9.7) are specified at the inlet boundaries. These freestream values were calculated from the facility stagnation pressure (P_{stag} = 350 psi) and temperature (T_{stag} = 1000 K) values specified in one of the representative tests. Equations relating the stagnation conditions to the freestream values are outlined in the literature.[26] In the simulations, the wedge was oriented at an angle of θ_{plate} = 5° and 1°. The bottom wall is specified as a no-slip condition, zero normal gradient in pressure and fixed temperature (T = 314 K). The fixed temperature was determined from the experimental data at this condition.[11] The right outflow boundary is specified as zero normal gradient for the temperature, velocity and pressure boundary conditions. There was a concern that the zero gradient pressure boundary condition would result in unwanted wave reflections at the outlet. After running the simulation it was found that as long as the oblique shockwave exits on the right boundary rather than the top boundary, no reflections were observed.

III. Sensitivity Results

Figure 4 shows the effect of grid cell spacing on distributions of temperature for the rhoCentralReactingFoam solver; Δ is the cell size and is taken at the center of the boundary layer. Initial simulations using the rhoCentralReactingFoam solver used a Δ = 0.1 mm in the vertical direction. This proved to be inadequate to properly resolve the boundary layer. The difference in predictions between simulations with grid spacing of 0.05 mm and 0.03 mm is negligible (< 0.1%). Therefore, the solution is independent of grid size when the spacing is smaller than 0.05 mm. The maximum Courant number was limited to 0.3 in the simulations. The simulation results were insensitive to the time step when the Courant number was below this value.

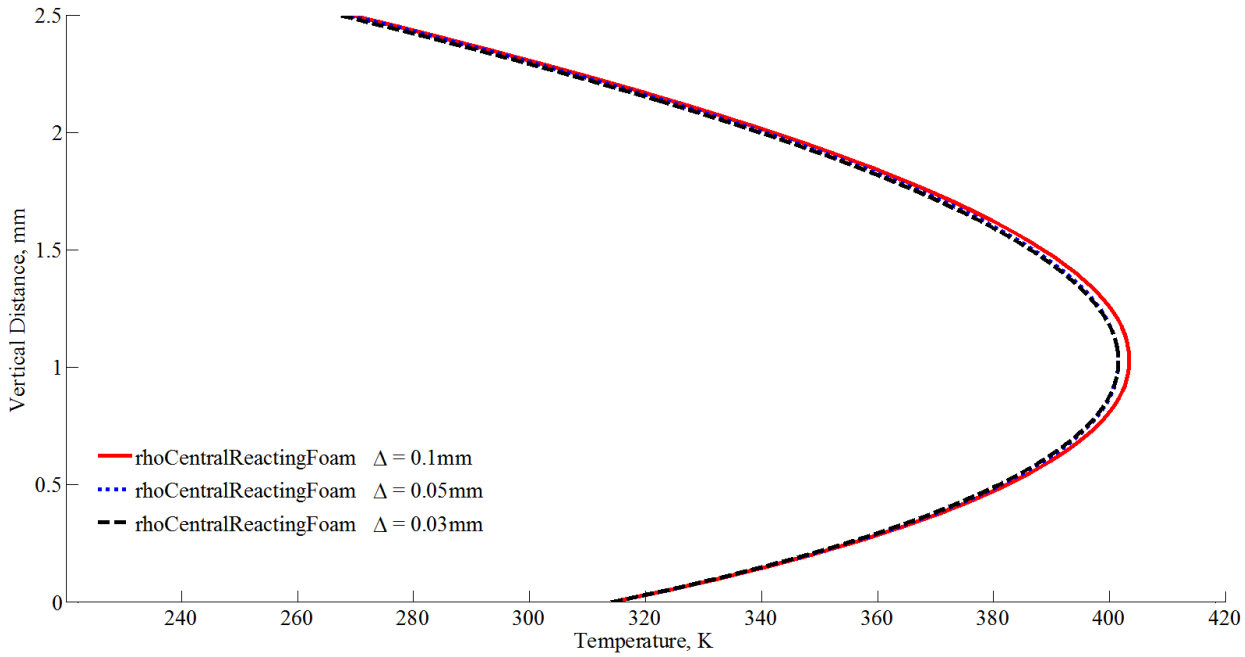

Figure 4. Grid convergence and boundary layer resolution. x = 106 mm downstream of leading edge.

Greenshields *et al.* recommends that a limited van Leer interpolation scheme be used when using rhoCentralFoam.[12] However, it was found that the use of the van Leer limiter results in an oscillatory solution, which is most noticeable for the x velocity in the post-shock region. Therefore, a Gamma differencing scheme was used instead as it maintained steep gradients near the shock but eliminated oscillations.[28] Figure 5 shows a plot of the x velocity along the x axis at approximately half the computational domain height (y = 15 mm) comparing the vanLeer limiter and Gamma differencing schemes. As can be seen from the figure, the vanLeer limited solution oscillated considerably; these oscillations did not decay as the simulation time increased.

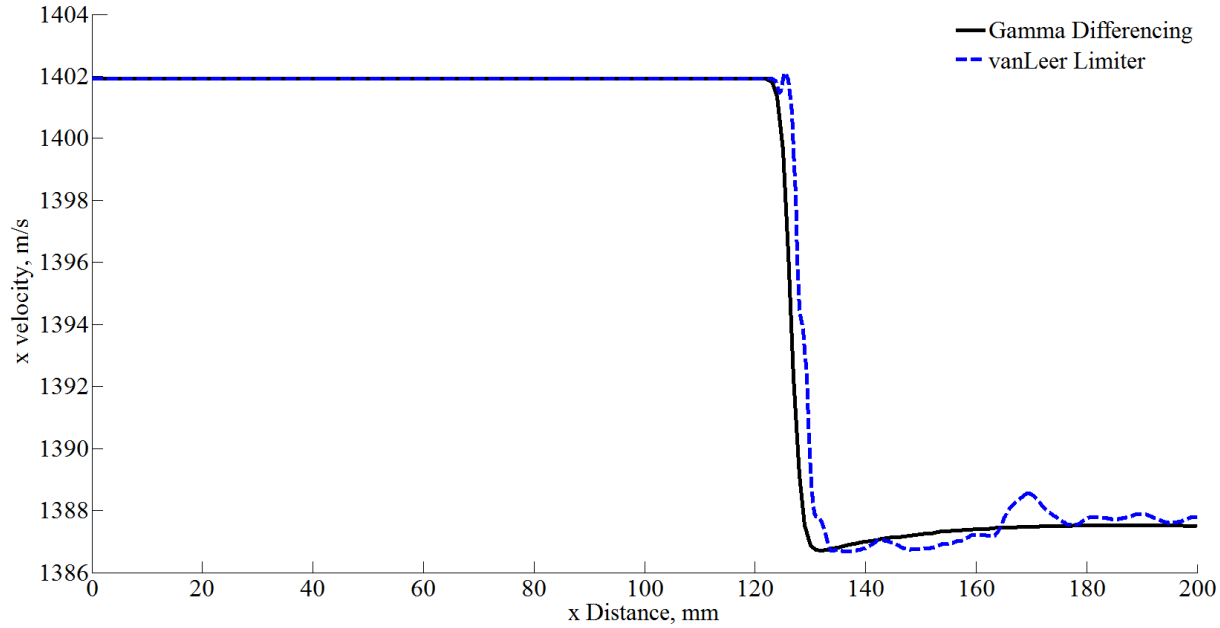

Figure 5. vanLeer Limiter and Gamma differencing numerical interpolation schemes for a 5 degree wedge, Pstag = 350psi; Tstag = 1000K.

IV. Comparison of CFD Solutions

Simulation results from rhoCentralReactingFoam are compared directly against previous ANSYS Fluent v6.3 results.[11] The Roe-FDS scheme was used for shock capturing in the ANSYS Fluent simulations. Figures 6 and 7 show comparisons of vertical distributions of Mach number and temperature for a case without gas seeding. Consistent with the previous work,[11] the vertical (y) distributions are displayed at a streamwise position of x = 106 mm downstream of the leading edge.

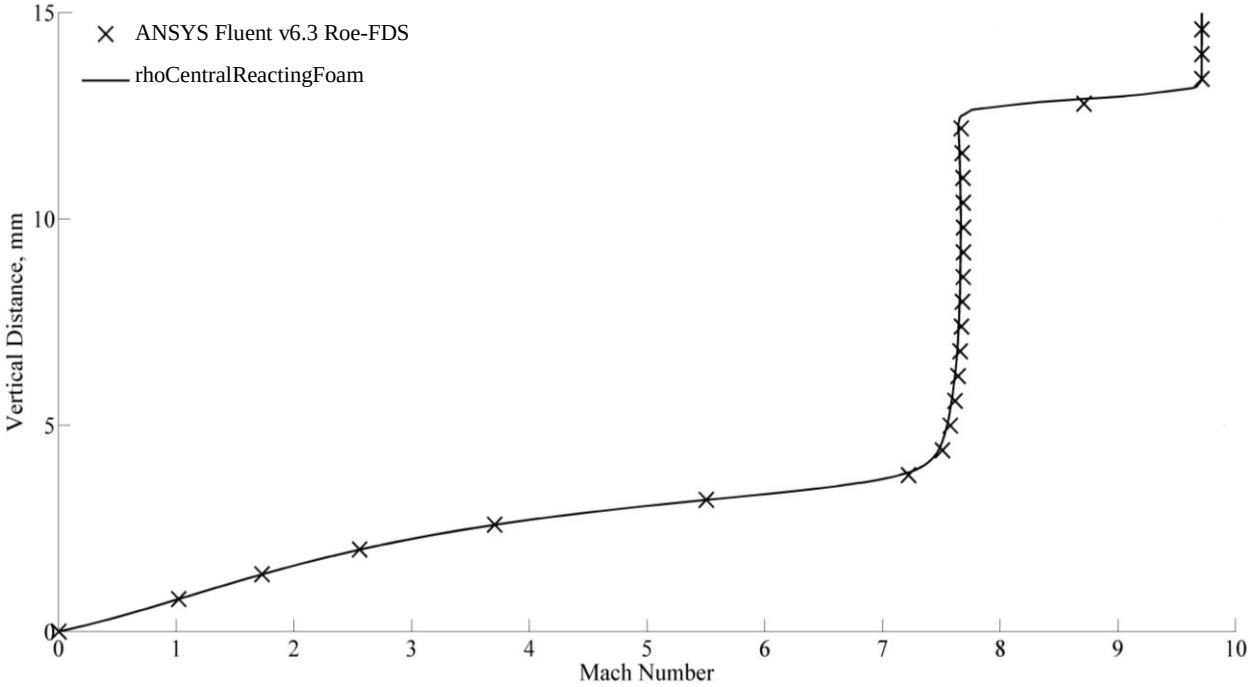

Figure 6. Vertical distributions of Mach number predicted by rhoCentralReactingFoam and ANSYS Fluent. x = 106 mm downstream of leading edge.

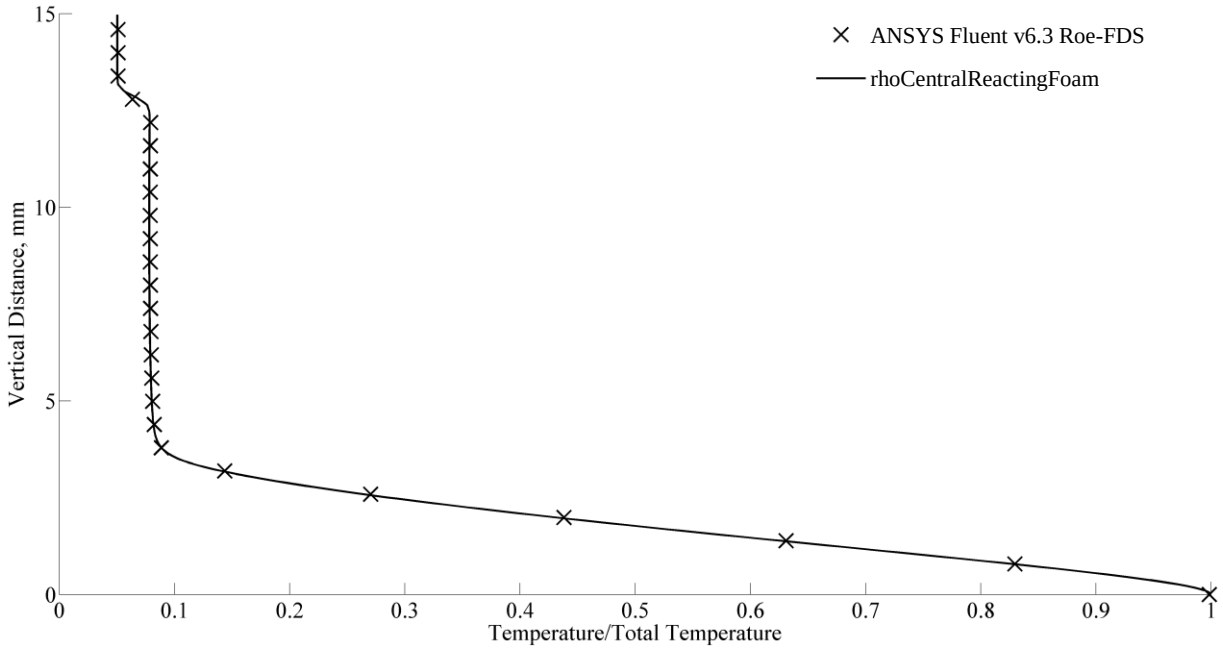

Figure 7. Vertical distributions of static temperature predicted by rhoCentralReactingFoam and ANSYS Fluent. x = 106 mm downstream of leading edge.

In general, there is good agreement between the rhoCentralReactingFoam code and ANSYS Fluent in predicting mean flow quantities. Fluent does predict a slightly sharper gradient at the oblique shock location; this is largely due to the fact that the mesh used for the Fluent results was dynamically refined. Since the region of interest in this study is near the boundary layer, which is far away from the oblique shock and the predictions before and after the shock show excellent agreement between the solvers, the difference is not a concern.

RhoCentralReactingFoam's multispecies diffusion model was also compared to ANSYS Fluent. Both solvers computed NO seeding into the boundary layer using the same freestream conditions in the non-seeding case. For this comparison, the NO mass flow rate was set to 3 μg/s, which is equivalent to 150 standard cubic centimeters per minute (sccm). This flow rate is typical for NO PLIF in this facility. The comparison can be seen in Fig. 8.

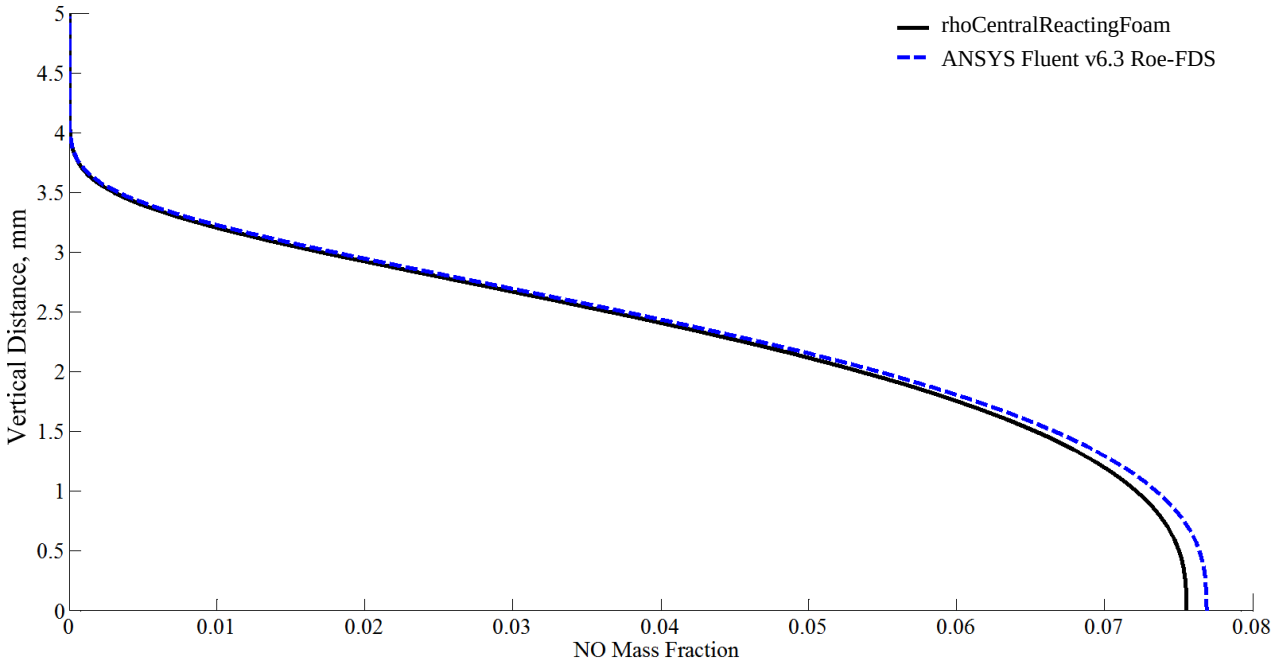

Figure 8. Vertical distributions of NO mass fraction predicted by rhoCentralReactingFoam and ANSYS Fluent. *x* = 106 mm downstream of leading edge. NO flow rate = 150 sccm

Small discrepancies (5%) are observed between the two solvers in predictions of NO mass fraction near the wall. This is caused by the difference in seed gas boundary type that was used. The ANSYS Fluent simulation used a mass flow inlet boundary condition directly at the bottom boundary of the region of interest. Implementing this type of boundary condition in OpenFOAM was unsuccessful as it resulted in non-physical predictions in NO mass flow rate. Instead, a two-dimensional inlet pipe with a length of four seed slot diameters was added to the computational domain in OpenFOAM. The pipe walls were specified as slip boundaries in an effort to match the ANSYS Fluent results, which did not include any wall losses upstream of the mass flow boundary. The OpenFOAM boundary condition is considered to be more accurate, as piping is used to connect the slot to a plenum inside the wedge model in the experiment. However, wall losses in the piping were not included in either simulation. Future simulations are planned to assess the effects of wall losses on the overall simulation results. The pipe walls were set to a constant static temperature of 314K. The total temperature of the pipe inflow boundary was set to 321 K which is equal to that of the ANSYS Fluent simulations.[11] The mass flow rate was kept constant at 150 sccm.

V. NO Chemistry

The static temperature in the test section of the 31-inch Mach 10 facility is low (~52 K) because of the large expansion that occurs in the nozzle. It is known that NO reacts with Oxygen (O_2) at low temperatures in a termolecular reaction to form nitrogen dioxide defined as:

$$O_2 + 2NO => 2(NO_2) \tag{10}$$

The reaction is of concern due to its rapidity at low temperatures and exothermic nature. The heat generated from the reaction has the potential to alter the thermodynamic properties of the boundary layer. The reaction rate has been measured experimentally by Olbregts.[29] An adapted version of his empirical formula in an Arrhenius rate form is given as:

$$k_{NO} = 10^{A} T^{B} \exp\left[\frac{E_a}{RT}\right] \tag{11}$$

where E_a is the activation energy given by

$$E_a = RCln(10) \tag{12}$$

A, *B*, and *C* are empirical constants with values of -5.18, 2.70 and 700, respectively. The formula given in Eq. (11) has units of liters^2 mols^{-2} seconds^{-1}. A plot of the reaction rate as a function of temperature can be seen in Fig. 9. The empirical formula is valid for temperatures between 226 K and 758 K.[29]

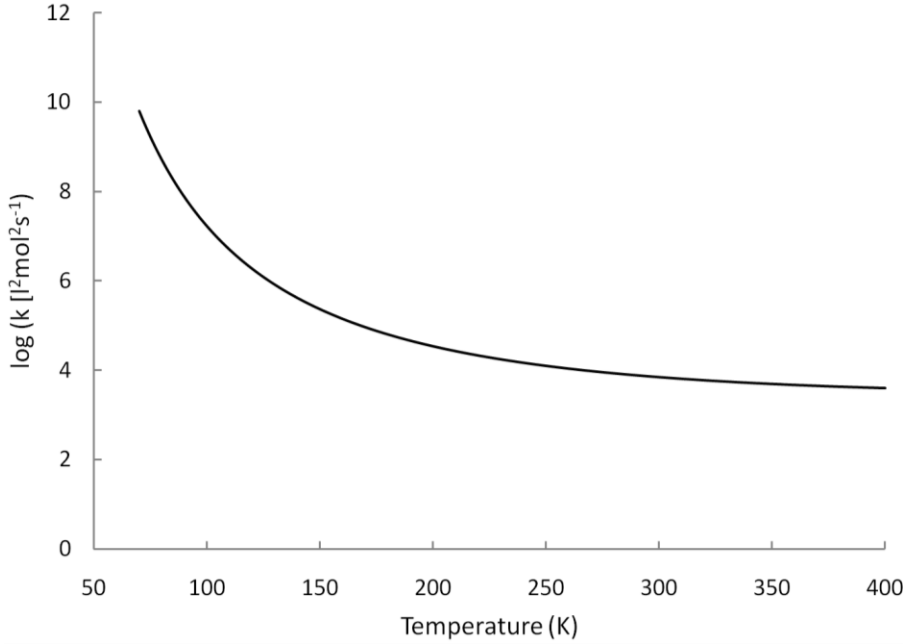

Figure 9. Effect of temperature on rate of reaction of NO.

In the following calculations, the reaction rate model was extrapolated to low temperatures to account for the relatively cold edge conditions near the edge of the boundary layer. However, the temperature in the boundary layer where most of the NO is concentrated is approximately 300 K to 400 K in the 5 degree case.

A. NO Half-life

The importance of NO chemistry in the flow was estimated through a half-life calculation. The half-life is then compared to the residence time of the flow based on analytical pressure, temperature, and velocity calculations. Finally, the half-life calculation is applied to CFD simulations with and without gas seeding. The change in NO concentration over time can be written as:

$$\frac{\mathrm{d[NO]}}{\mathrm{dt}} = -2\mathrm{k_{NO}}[\mathrm{O_2}][\mathrm{NO}]^2 \tag{13}$$

If the concentration of O_2 is assumed to be constant, the variables can be separated and Eq. (13) becomes:

$$\frac{d[NO]}{[NO]^2} = -2k_{NO}[O_2]dt \tag{14}$$

Integrating Eq. (14) from $[NO]_i$ to $[NO]_f$ where $[NO]_f$ is equal to $0.5[NO]_i$ yields:

$$-\frac{2}{[NO]_i} - \frac{1}{[NO]_i} = 2k_{NO}[O_2]t_{1/2} \tag{15}$$

Solving Eq. (15) for $t_{1/2}$ results in:

$$t_{1/2} = \frac{1}{2k_{NO}[O_2][NO]_i} \tag{16}$$

The concentrations of NO and O_2 can be written as:

$$[NO] = X_{NO}\left(\frac{P}{RT}\right) \tag{17}$$

$$[O_2] = X_{O_2}\left(\frac{P}{RT}\right) \tag{18}$$

Substituting Eq. (17) and Eq. (18) into Eq. (16) results in:

$$t_{1/2} = \frac{R^2T^2}{2k_{NO}X_{NO,i}X_{O_2}P^2} \tag{19}$$

If the concentration of O_2 is not assumed constant, the change in O_2 concentration over time can be written as:

$$\frac{d[O_2]}{dt} = -k_{NO}[O_2][NO]^2 \tag{20}$$

Substituting Eq. (20) into Eq. (13) gives:

$$\frac{d[O_2]}{dt} = \frac{1}{2}\frac{d[NO]}{dt} \tag{21}$$

Since O_2 is in excess for the experimental setup $[O_2]$ can be written as:

$$[O_2] = [O_2]_u + [O_2]_e \tag{22}$$

Where $[O_2]_u$ is the concentration of O_2 used by the reaction and $[O_2]_e$ is the excess concentration of O_2. From Eq. (10) the ratio of NO to O_2 used can be obtained. Solving Eq. (22) for $[O_2]_u$ and substituting into this ratio results in:

$$\frac{[NO]}{[O_2] - [O_2]_e} = 2 \tag{23}$$

Solving Eq. (23) for $[O_2]$ and substituting into Eq. (13) yields:

$$\frac{d[NO]}{dt} = -2k_{NO}\left(\frac{[NO]^3}{2} + [NO]^2[O_2]_e\right) \tag{24}$$

Separating variables results in:

$$\frac{d[NO]}{\frac{[NO]^3}{2} + [NO]^2[O_2]_e} = -2k_{NO}dt \tag{25}$$

Since $[O_2]_e$ is a constant, Eq.(25) can be integrated:

$$-2k_{NO}t_{1/2} = \frac{[NO]_i \ln\left[\frac{[NO]_i + 4[O_2]_e}{[NO]_i + 2[O_2]_e}\right] - 2[O_2]_e}{2[O_2]_e^2[NO]_i} \tag{26}$$

Knowing that the excess concentration of O_2 is equal to the initial concentration less the used concentration and that the ratio of O_2 used to NO is equal to two; the excess concentration of O_2 can be written as:

$$[O_2]_e = [O_2]_i - \frac{1}{2}[NO]_i \tag{27}$$

From Eq. (17) and Eq. (18), Eq. (27) can be written as:

$$[O_2]_e = \left(X_{O2,i} - \frac{1}{2}X_{NO,i}\right)\left(\frac{P}{RT}\right) \tag{28}$$

Substituting Eq. (20) and Eq. (28) into Eq. (26) and solving for $t_{1/2}$ results in:

$$t_{1/2} = \frac{X_{NO,i}\left(1 + \ln\left[\frac{4X_{O2,i} - X_{NO,i}}{2X_{O2,i}}\right]\right) - 2X_{O2,i}}{-k_{NO}\left(2X_{O2,i} - X_{NO,i}\right)} \tag{29}$$

A sample plot showing the concentration of NO over time for T = 300 K and P = 300 Pa, which is representative of the flow inside the boundary layer, can be seen in Fig. 10. These results were obtained from an initial O_2 mol fraction of 0.2 and an initial NO mol fraction of 0.1. It should be noted that the shortest half-life is predicted by the constant O_2 assumption, which is expected.

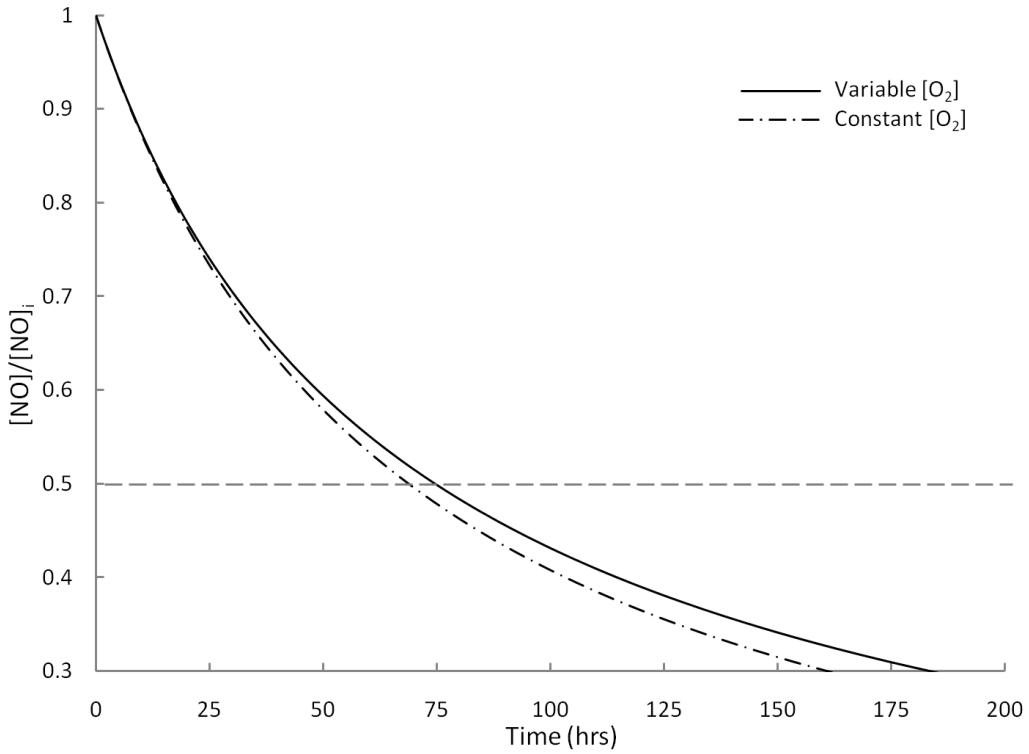

Figure 10. Effect of O_2 concentration on rate of reaction of NO based on Eq. (17) and (30). P = 300 Pa, T = 300 K.

Once the half-life of NO is known it can be compared to residence time in the computational domain. If the half-life is long compared to the residence time of the flow then the flow can be approximated as non-reacting. Figures 11 and 12 show contour plots of temperature and pressure obtained from the OpenFOAM simulation. Pressure and temperature are directly related to reactant concentration and reaction rate. Figure 13 shows the ratio of half-life length scale ($L_{1/2}$) normalized by the local simulation length scale (L_{sim}):

$$\frac{L_{1/2}}{L_{sim}} = \frac{U_x * t_{1/2}}{L_d - x} \tag{30}$$

where U_x is the x velocity, L_{sim} is the length of the computational domain and x is the horizontal distance from the origin (leading edge). Because of the large range in $L_{1/2}$ calculations, Fig. 13 is shown on a log scale. The half-life length scale was chosen since the reaction is asymptotic at low NO concentrations. It provides an order of magnitude analysis. A large value of $L_{1/2}/L_{sim}$ indicates that the flow is non-reacting.

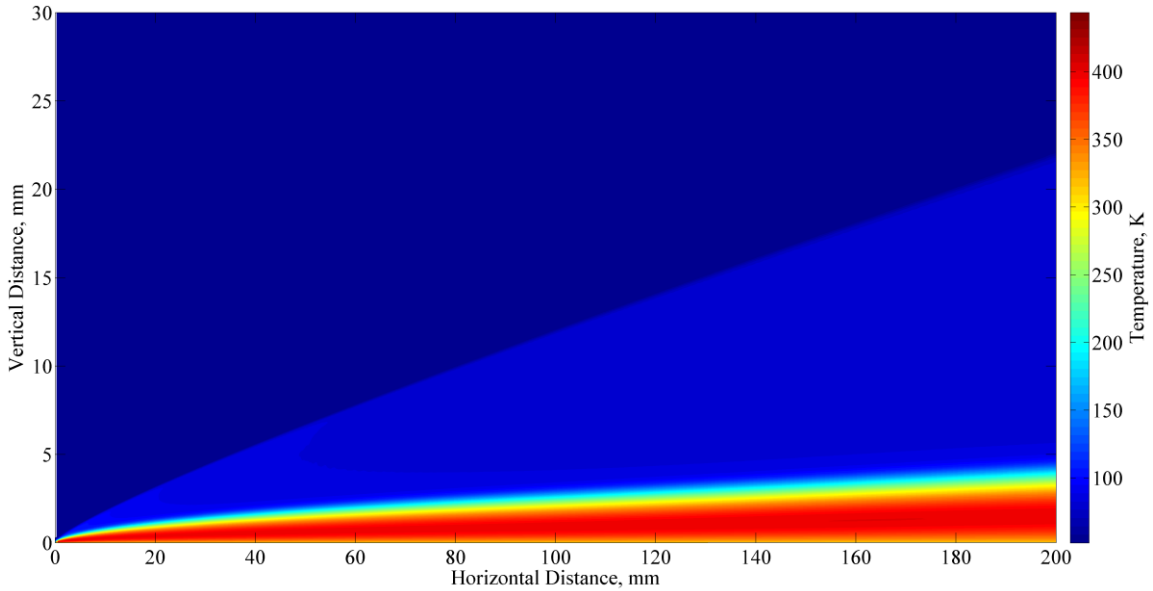

Figure 11. Simulated temperature distribution. P_{stag} = 350 psi; T_{stag} = 1000 K; θ_{plate} = 5°.

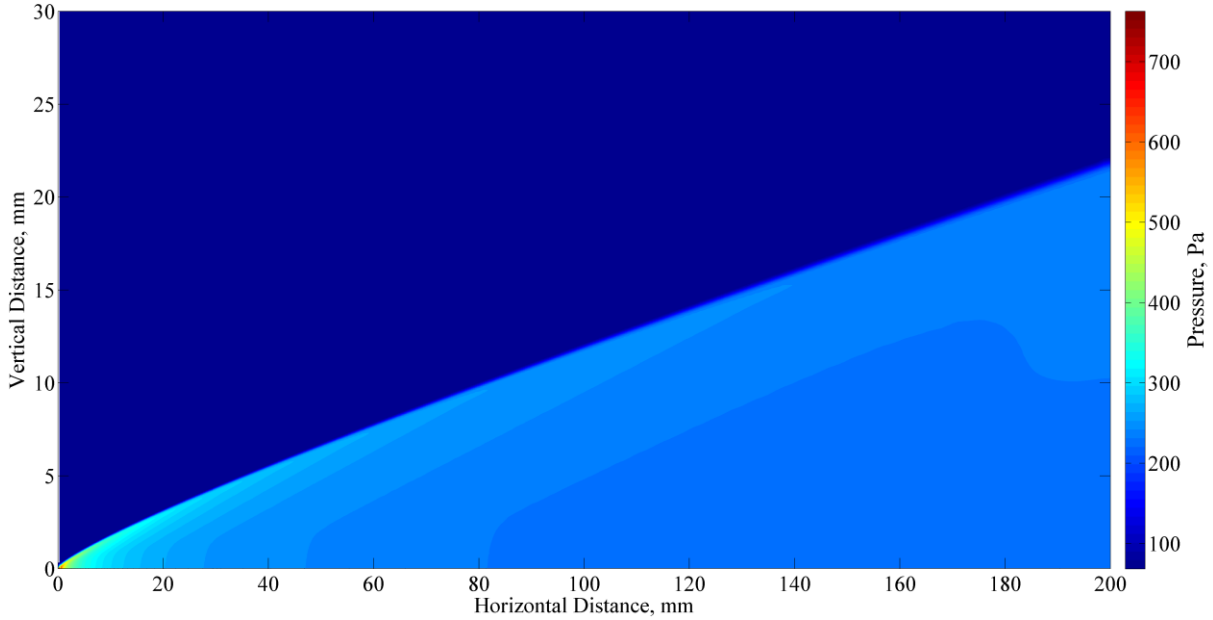

Figure 12. Simulated pressure distribution. P_{stag} = 350 psi; T_{stag} = 1000 K; θ_{plate} = 5°.

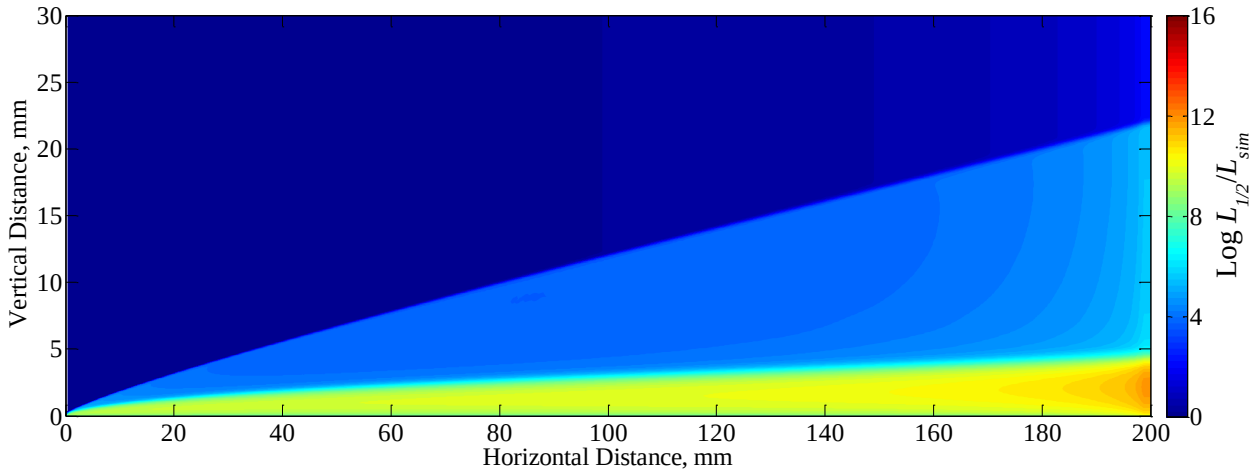

Figure 13. Simulated $L_{1/2}/L_{SIM}$ distribution based on Eq. (30) P_{stag} = 350 psi; T_{stag} = 1000 K; θ_{plate} = 5° ; $X_{NO,i}$ = 0.1; $X_{O2,i}$ = 0.2.

The minimum value of the $L_{1/2}/L_{SIM}$ ratio is 0.84 and occurs in the freestream at the computational domain inlet where the temperature is 52 K. This indicates that if NO was present in the freestream, it would react within the computational domain. However, NO is seeded within the boundary layer and is unable to penetrate much beyond the velocity boundary layer, which is far away from the leading shock wave. Therefore, the lowest expected value of $L_{1/2}$ is at the edge of the boundary layer, which roughly corresponds to the edge conditions after the oblique shock wave. The pressure and temperature conditions at this location can be found from the oblique shock relations.[30]

The minimum half-life length scale for different wedge angles and wind tunnel stagnation conditions can then be estimated from the post-shock conditions and Eq. (29). The results, over the range of typical stagnation pressures in NASA Langley's 31" Mach 10 facility, can be seen in Fig. 14. Cases which have been simulated are indicated with filled-in dots. From the figure it can be seen that the NO reaction has the potential to alter the thermodynamic characteristics at shallower wedge angles and at higher stagnation pressures. The dashed line indicates the position $L_{1/2}/L_{sim}$ = 1 and corresponds to the approximate limit where NO reactions will occur within the field of view of the wedge model or computational domain. Two major assumptions are that the NO concentration boundary layer is thicker than the thermal boundary layer and that the Olbregts reaction can be reliably extrapolated to these lower temperatures.

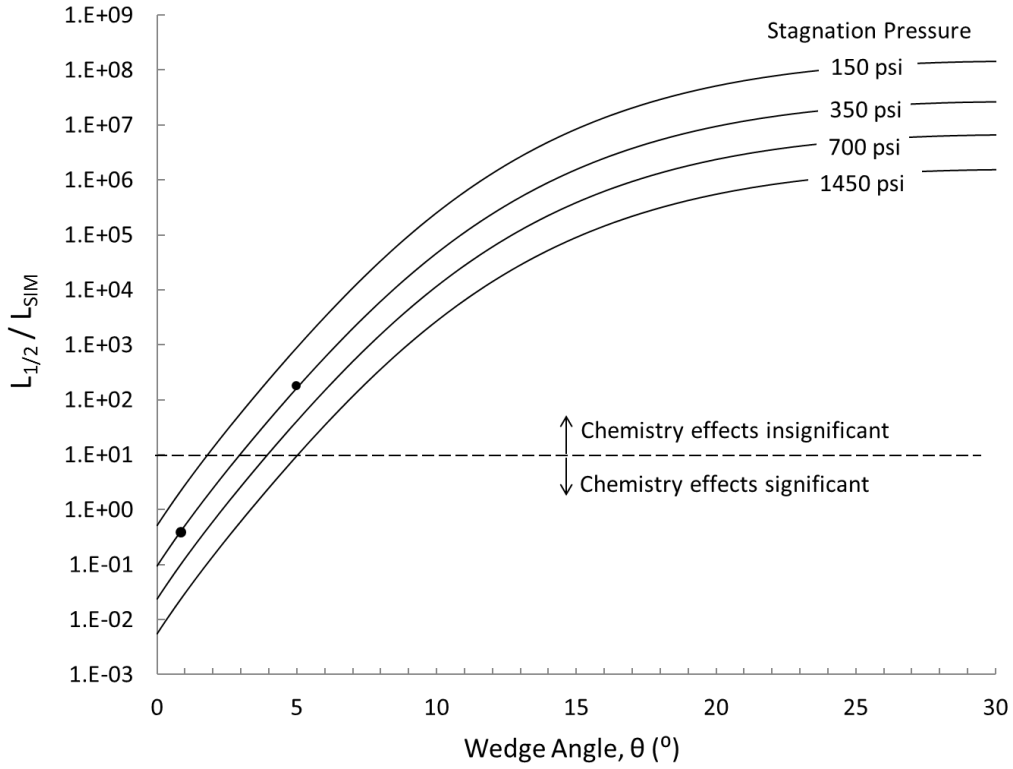

Figure 14. Effect of NASA's 31" Mach 10 facility stagnation pressure on the length scales of NO chemistry. Eq. (30) used for $L_{1/2}$ calculation.

To account for non-uniform NO distributions, life time calculations were performed on gas seeding simulations without chemical reactions. Figure 15 shows the distribution of $L_{1/2}$ based on the simulated NO gas seeding case performed using the rhoCentralReactingFoam solver at a wedge angle of θ_{plate} = 5° and an NO seed rate of 150 sccm. The color scheme has been changed from the previous figures to better accentuate the regions where $L_{1/2}$ is at a minimum.

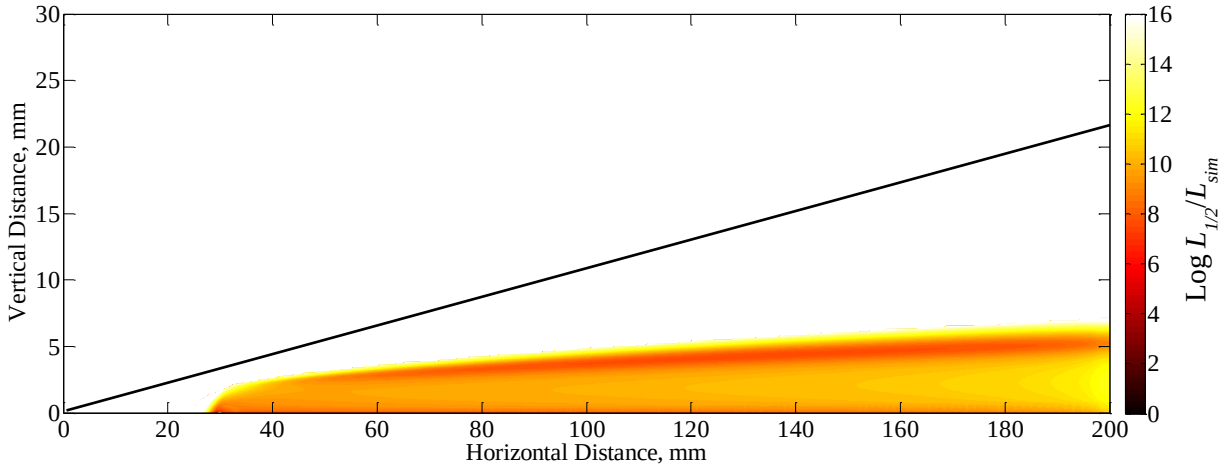

Figure 15. $L_{1/2}/L_{SIM}$ distribution based on simulated NO gas seeding and Eq. (30).

With gas seeding, the concentration of NO is the largest near the injection slot where the gas temperature is near the wall temperature (314 K). Although the NO reaction rate coefficient, k_{NO}, is large at the edge of the boundary layer, concentration levels of NO decrease such that $L_{1/2}$ values effectively increase. Since there is negligible NO concentration levels outside of the boundary layer, the $L_{1/2}/L_{sim}$ contours were cropped at those locations. The solid line in the figure shows the location of the oblique shock wave for reference. Minimum $L_{1/2}$ values occur in the

immediate vicinity of the injection slot where the concentration of NO is highest. The next lowest values are near the edge of the boundary layer, where the temperature is low.

B. Reacting Simulations

Simulations of NO gas seeding with chemical reactions were performed with rhoCentralReactingFoam at a plate angle of 5 degrees and a stagnation pressure of 350 psi. A contour plot of the NO_2 mass fraction can be seen in Fig. 16. As expected, the majority of reactions occur at the seeding slot. NO_2 produced there convects and disperses downstream, accumulating at the edge of the concentration boundary layer. Reactions are also observed at the edge of the boundary layer, further increasing the NO_2 concentration levels.

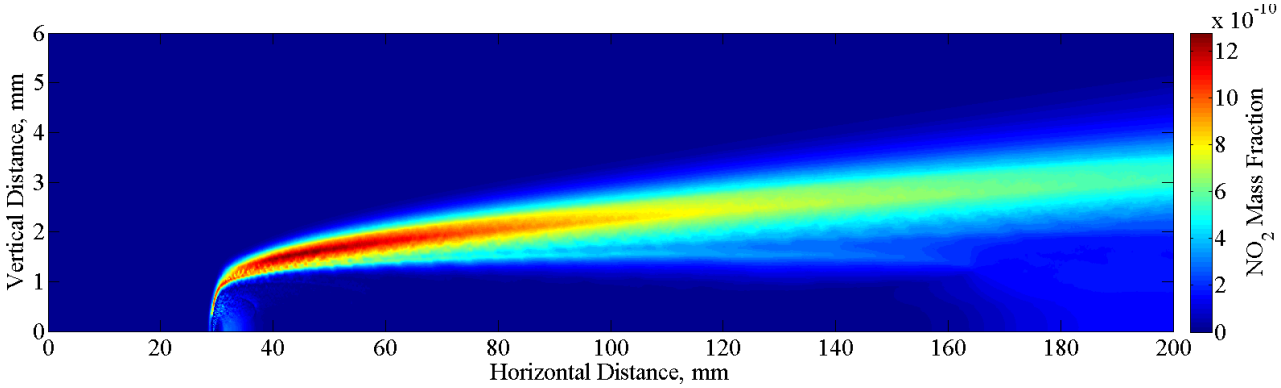

Figure 16. Simulated NO_2 distribution P_{stag} = 350 psi; T_{stag} = 1000 K; θ_{plate} = 5° ;

Simulations at lower plate angles, which reduces the edge static temperature, were performed to increase the magnitude of chemistry effects on the overall flow field. The predicted NO_2 contours for θ_{plate} = 1° can be seen in Fig. 17. Since concentration levels of NO decrease rapidly downstream of the seeding slot, the effect of chemical reactions on the flow is negligible at all positive plate angles. Negative plate angles were not simulated in this study. However, small aerodynamic perturbations in the boundary layer were observed as a result of the NO injection. This effect was already demonstrated in a previous study of non-reacting gas seeding simulations.[11]

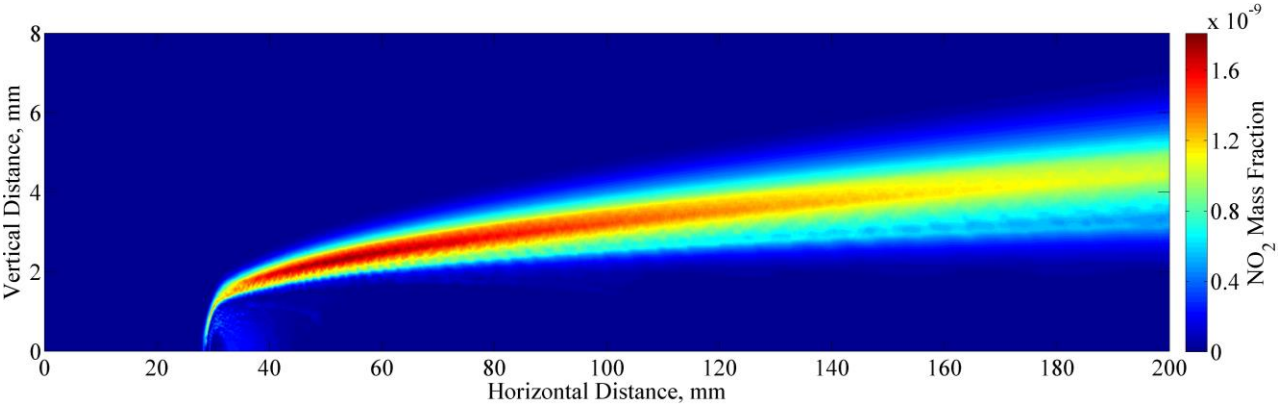

Figure 17. Simulated NO_2 distribution P_{stag} = 350 psi; T_{stag} = 1000 K; θ_{plate} = 1° ;

Although it was determined that the effects of NO chemical reactions on the flow are negligible at all positive plate angles, it is of interest to study the adverse chemistry effects that would occur if the reaction rate were higher. Therefore, the reaction rate was artificially increased by a factor of 1000 for the θ_{plate} = 1° condition. All of the other flow conditions were kept constant. Predictions of NO_2 and temperature distributions are shown in Fig. 18. Larger amounts of NO_2 are produced downstream of the seeding slot and are distributed throughout the boundary layer. Small amounts of NO_2 are observed at the very edge of the boundary layer where the temperatures are very low.

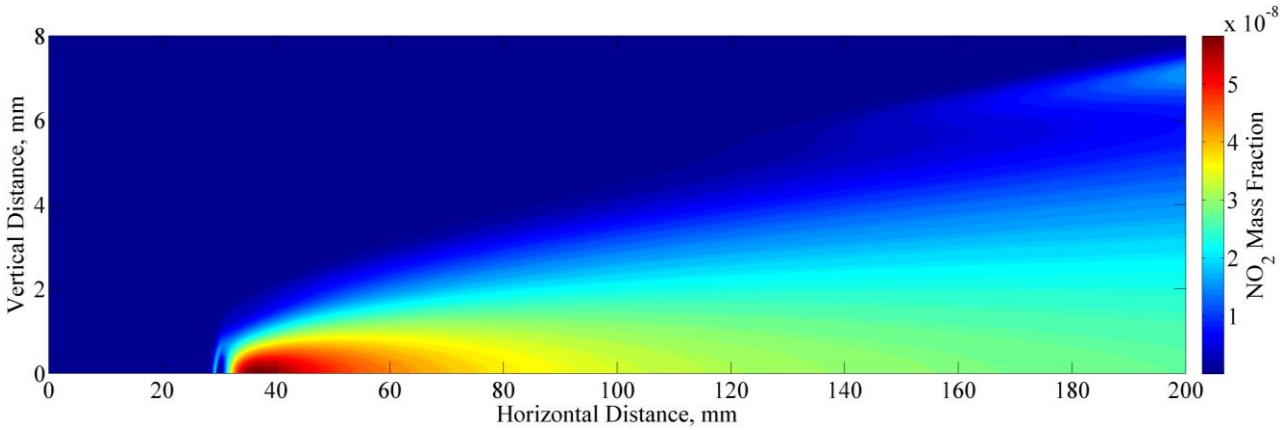

Figure 18. Simulated NO_2 distribution P_{stag} = 350 psi; T_{stag} = 1000 K; θ_{plate} = 1°; Reaction rate increased by a factor of 1000;

VI. Discussion

When comparing vertical distributions of NO_2 and the reaction rate for the θ_{plate} = 5° and θ_{plate} = 1° cases, it is evident that while NO is present near the edge of the boundary layer, it does not react in significant quantities at that location. The bulk of the reactions take place near the seed jet outlet where the concentration of NO is highest. The temperature difference due to the heat released by the chemical reaction in the vicinity of the seeding slot was found to be less than 0.5% compared to the nonreactive simulation temperature for both cases.

Figure 19 shows the vertical distribution of NO_2 for the 5° wedge simulation at x = 106 mm downstream of the leading edge. $L_{sim}/L_{1/2}$ values are taken from Figure 15 and represent the predicted values based on the simulation without reactions. The inverse of $L_{1/2}/L_{sim}$ was shown so that the plots could be more readily compared to each other. A peak in the $L_{sim}/L_{1/2}$ plot corresponds to a minimum half-life of NO. It can be seen that the NO_2 peak has little correlation to the $L_{sim}/L_{1/2}$ plot. If the NO reaction took place near the edge of the boundary layer in noticeable quantities, the vertical position of the two peaks would be closer together. A plot tracking the y coordinate of the peak NO_2 concentration and $L_{sim}/L_{1/2}$ values can be seen in Fig. 20. The $L_{sim}/L_{1/2}$ plot starts at around x = 45 mm from the leading edge as the $L_{sim}/L_{1/2}$ peaks are not well defined upstream of that position. This is caused by the close proximity to the seed slot. The low half-life near the seed slot shifts the $L_{sim}/L_{1/2}$ peak from the within the boundary layer to the wall surface. However, it can be seen that the two peaks approach each other as the distance from the seed slot decreases. This is consistent with the idea that the bulk of the chemical reactions take place near the seed slot where the concentration of NO is the highest.

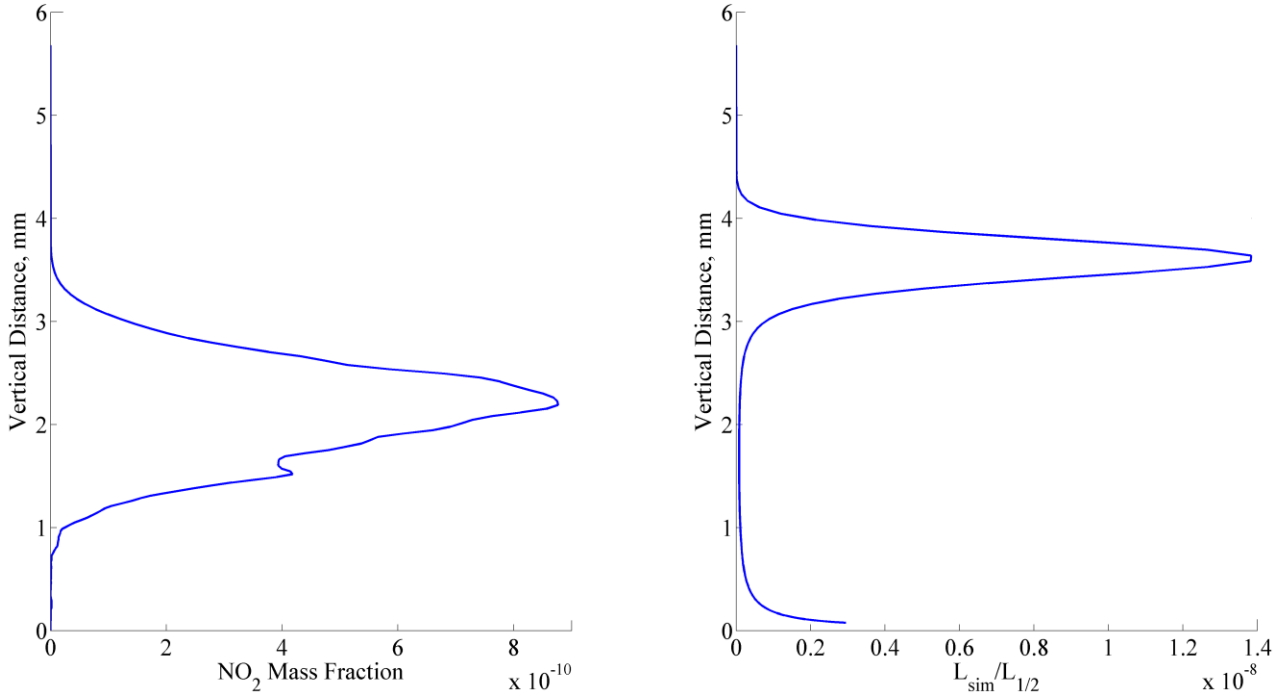

Figure 19. Vertical distributions of NO_2 mass fraction (left) and $L_{sim}/L_{1/2}$ (right). *x* = 106 mm downstream of leading edge. P_{stag} = 350 psi; T_{stag} = 1000 K; θ_{plate} = 5° ;

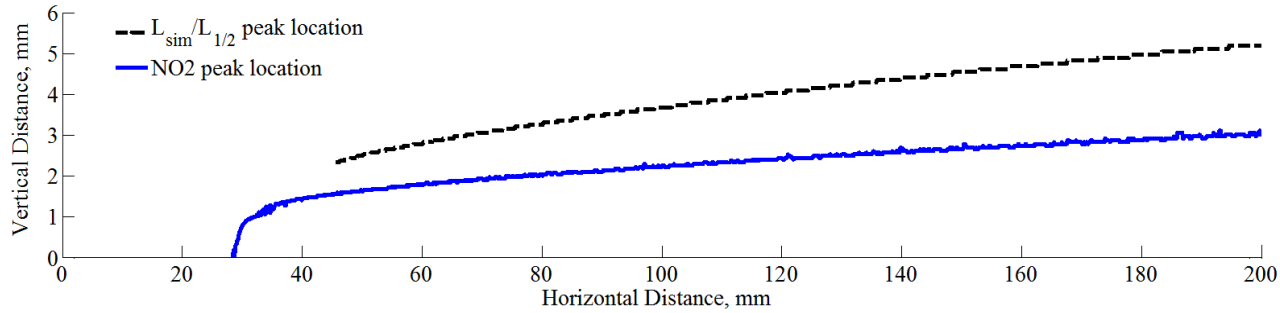

Figure 20. Stream wise positions of peak NO_2 mass fraction and $L_{sim}/L_{1/2}$ P_{stag} = 350 psi; T_{stag} = 1000 K; θ_{plate} = 5° ;

The analytical model for NO chemistry, the results of which are shown in Fig. 14, indicates that the edge conditions for the θ_{plate} = 1° case will result in a static temperature low enough such that chemistry effects will be important. This model assumes that NO escapes beyond the thermal boundary layer and is exposed to the edge conditions. In contrast, simulations with variable NO indicate that the bulk of reactions take place near the seeding slot boundary, where the static temperature is much higher. While the conditions outside of the boundary layer are favorable for the NO reaction to take place, NO does not penetrate beyond the thermal boundary layer. In addition, the concentration of NO at the edge of the boundary layer is low enough such that only a negligible amount of NO_2 forms. While more NO_2 is produced when the wedge angle is decreased, significant quantities fail to form.

For significant reactions to occur, the concentration boundary layer would need to be thicker than the thermal boundary layer. It was shown in the previous work[11] that this was not the case for θ_{plate} = 5°. Results here indicate that this is also not the case for θ_{plate} = 1°. The only conditions where reaction rates could be of importance are at higher seed flow rates and at negative wedge angles where Prandtl-Meyer expansion would cause a decrease in temperature.

Simulations with artificially amplified reaction rates help to assess the uncertainty involved in extrapolating Olbregt's NO reaction rate to low temperatures (< 226 K). Even with an extremely amplified reaction rate, simulations show that the chemistry effects are still negligible. Although small in magnitude, the distribution of NO_2

concentration levels change when the reaction rate is artificially amplified. As expected, more NO_2 is produced inside the boundary layer but most of the NO_2 is still produced is near the jet slot.

VII. Conclusion

The local concentration levels of NO and O_2 are the main factor that drives the reaction of NO seeded into a hypersonic boundary layer on a wedge model at positive angles of attack in NASA Langley's 31-inch Mach 10 facility. Large magnitudes of the local reaction rate coefficient driven by low static temperatures at the edge of the boundary layer are counter balanced by low concentrations of NO; as a result the reaction rate was found to be negligible for wedge angles greater than and equal to 1^{o} and with an NO seed rate of 150 sccm or less. While some NO_2 is produced in the boundary layer at these conditions, the total amount of heat produced due to chemical reactions is negligible. Half-life predictions based on uniform NO concentration levels are not reliable in predicting the importance of chemistry effects for locally seeded flows. NO has a very high dispersal rate but is unable to penetrate beyond the thermal boundary layer, resulting in negligible chemical reactions. Simulations with artificially high reaction rates indicate that large reactions would mainly occur near the wall and extrapolation of Olbregt's empirical formula below 226 K is unnecessary to predict the reacting flow. Even with the reaction rate amplified by a factor of 1000, reactions of NO had a negligible impact on the boundary layer flow properties at these conditions.

Acknowledgments

The authors would like to thank Jeff Balla and Paul Danehy for providing valuable information regarding the half-life calculations, wind tunnel experiment, and the laser imaging setup. This work was supported by the Natural Sciences and Engineering Research Council of Canada (NSERC).

References

[1] T.J. Horvath, S.A. Berry, N.R. Merski, K.T. Berger, G.M. Buch, D.S. Liechty, and S.P. Schneider, "Shuttle damage/repair from the perspective of hypersonic boundary layer transition – experimental results," AIAA 2006-2919, *9th AIAA/ASME Joint ThermoPhysics and Heat Transfer Conference*, San Francisco, CA, June 2006.

[2] S.P. Schneider, "Effects of Roughness on Hypersonic Boundary-Layer Transition," *Journal of Spacecraft and Rockets*, Vol 45, No. 2, 2008, pp. 193-209.

[3] W.S. Saric, "Görtler Vorticies," Annual Review of Fluid Mechanics, Vol. 26, 1994, pp. 379-409.

[4] L.M. Mack, "Boundary Layer Linear Stability Theory," Report 709, Special Course on Stability and Transition of Laminar Flow, AGARD, March 1984, pp. 1-81.

[5] W. S. Saric, H.L. Reed, and E.B. White, "Stability and Transition of Three-Dimensional Boundary Layers," *Annual Review of Fluid Mechanics*, Vol. 35, 2003, pp. 413-330.

[6] D. Arnal and G. Casalis, "Laminar-Turbulent Transition Prediction in Three-Dimensional Flows," *Process in Aerospace Sciences*, Vol. 36, No. 2, Feb. 2000, pp. 173-191.

[7] T. Medford, P. M. Danehy, S. B. Jones, B. F. Bathel, J. A. Inman, N. Jiang, M. Webster, W. Lempert, J. Miller, and T. Meyer, "Stereoscopic Planar Laser-Induced Fluorescence Imaging at 500 kHz," AIAA 2011-985, *49th AIAA Aerospace Sciences Meeting including the New Horizons Forum and Aerospace Exposition*, Orlando, Florida, January 2011.

[8] B. F. Bathel, P. M. Danehy, J. A. Inman, A. N. Watkins, S. B. Jones, W. E. Lipford, K. Z. Goodman, C. B. Ivey, and C. P. Goyne, "Hypersonic Laminar Boundary Layer Velocimetry with Discrete Roughness on a Flat Plate," AIAA 2010-4998, *40th AIAA Fluid Dynamics Conference and Exhibit*, Chicago IL, June 2010.

[9] P.M. Danehy, C. B. Ivey, J.A. Inman, B. Bathel, S.B. Jones, A. C. McCrea, N. Jiang, M. Webster, W. Lempert, J. Miller, and T. Meyer "High-speed PLIF imaging of hypersonic transition over discrete cylindrical roughness," AIAA 2010-0703, *48th AIAA Aerospace Sciences Meeting, Fluid Dynamics TC*, Orlando Florida, January 2010.

[10] P.M. Danehy, C. B. Ivey, B. F. Bathel, J.A. Inman, S.B. Jones, A. N. Watkins, K. Goodman, A. C. McCrea, B, D. Leighty, W. K. Lipford, N. Jiang, M. Webster, W. Lempert, J. Miller, and T. Meyer, "Orbiter BLT flight experiment wind tunnel simulations: nearfield flow imaging and surface thermography," AIAA-2010-1571, *48th AIAA Aerospace Sciences Meeting*, Orlando Florida, January 2010.

[11] C.T. Johansen, and P.M. Danehy, "Numerical Investigation of PLIF Gas Seeding for Hypersonic Boundary Layer Flows," *50th AIAA Aerospace Sciences Meeting Including the New Horizons Forum and Aerospace Exposition*, Nashville, Tennessee, January 2012.

[12] C.J. Greenshields, H.G. Weller, L. Gasparini, and J.M. Reese, "Implementation of semi-discrete, non-staggered central schemes in a collocated, polyhedral, finite volume framework, for high-speed viscous flows," *International Journal of Numerical Methods in Fluids*, Vol. 63, 2010, pp. 1-21.

[13] H. Nessyahu and E. Tadmor, "Non-oscillatory central differencing for hyperbolic conservation laws," *Journal of Computational Physics*, Vol. 87, 1990, pp. 408–447.

[14] A. Kurganov and E. Tadmor, "New high-resolution central schemes for nonlinear conservation laws and convection–diffusion equations," *Journal of Computational Physics*, Vol. 160, 2001, pp. 241–282.

[15] B. van Leer, "Towards the ultimate conservative difference scheme, V: a second-order sequel to Godunov's method," *Journal of Computational Physics*, Vol. 32, 1979, pp. 101–136.
[16] P. Colella and P. Woodward, "The piecewise parabolic method (PPM) for gas-dynamical simulations," *Journal of Computational Physics*, Vol. 54, 1984, pp. 174–201.
[17] A. Harten, B. Engquist, S. Osher, and S.R. Chakravarthy, "Uniformly high order accuracy essentially non-oscillatory schemes III," *Journal of Computational Physics*, Vol. 71, 1987, pp. 231–303.
[18] X. D. Liu, S. Osher, and T. Chan, "Weighted essentially non-oscillatory schemes," *Journal of Computational Physics*, Vol. 115, 1994, pp. 200–212.
[19] B. Cockburn and C.W. Shu, "The Runge–Kutta discontinuous Galerkin method for conservation laws, V: multidimensional systems," *Journal of Computational Physics*, Vol. 141, 1998, pp.199–224.
[20] A. Bansal, A. Feldick, and M. F. Modest, "Simulation of Hypersonic Flow and Radiation over a Mars Reentry Vehicle Using OpenFOAM," *50th AIAA Aerospace Sciences Meeting including the New Horizons Forum and Aerospace Exposition*, Nashville, Tennessee, January 2012.
[21] M. Chapuis, C. Fureby, E. Fedina, N. Alin, and J. Tegnér, "LES Modeling of Combustion Applications Using OpenFOAM," *V European Conference on Computational Fluid Dynamics*, Lisbon, Portugul, June 2010.
[22] Y. Afarin, S. Tabejamaat, and A. Mardani, "Large Eddy Simulation Study of H2/CH4 Flame Structure at MILD Condition," *Seventh Mediterranean Combustion Symposium*, Sardinia, Italy, September 2011.
[23] R.S. Brodkey and H.C. Hershey, *Transport Phenomena, A Unified Approach*, McGraw-Hill Chemical Engineering Series, 1988.
[24] P.D. Neufeld, A.R. Janzen, and R.A. Aziz, "Empirical equations to calculate 16 of the transport collision integrals for the Lennard-Jones (12-6) potential," *Journal of Chemical Physics*, Vol. 57, Issue 3, 1972, pp. 1100-1102.
[25] R.A. Svehla, "Estimated viscosities and thermal conductivities of gases at high temperatures," NASA Technical Report R-132, 1962.
[26] Hollis, "Real-gas flow properties of NASA Langley Research Center aerothermodynamics facilities complex wind tunnels," NASA Contractor Report 4755, 1996.
[27] NIST-JANAF Thermochemical Tables, http://kinetics.nist.gov/janaf/, [retrieved May 19, 2011].
[28] H. Jasak, H.G Weller, and A.D. Gosman, "High Resolution NVD Differencing Scheme for Arbitrarily Unstructured Meshes," *International Journal For Numerical Methods in Fluids*, Vol. 31, 1999, pp.431-449.
[29] J. Olbregts, "Thermolecular Reaction of Nitrogen Monoxide and Oxygen: A Still Unsolved Problem," *International Journal of Chemical Kinetics*, Vol. 17, 1985, pp. 835-848.
[30] J.E. John and T.G. Keith, *Gas Dynamics*, Pearson Prentice Hall, 3rd Edition, 2006.